Detecting Baryon Acoustic Oscillations with Third-generation Gravitational Wave Observatories

Sumit Kumar[1,2] , Aditya Vijaykumar[3] , and Alexander H. Nitz[1,2]
[1] Max-Planck-Institut für Gravitationsphysik (Albert-Einstein-Institut), D-30167 Hannover, Germany; sumit.kumar@aei.mpg.de
[2] Leibniz Universität Hannover, D-30167 Hannover, Germany
[3] International Centre for Theoretical Sciences, Tata Institute of Fundamental Research, Bangalore 560089, India

Abstract

We explore the possibility of detecting baryon acoustic oscillations (BAO) solely from gravitational wave (GW) observations of binary neutron star mergers with third-generation (3G) GW detectors such as the Cosmic Explorer and the Einstein Telescope. These measurements would provide a new independent probe of cosmology. The detection of the BAO peak with current-generation GW detectors (solely from GW observations) is not possible because i) unlike galaxies, the GW mergers are poorly localized, and ii) there are not enough merger events to probe the BAO length scale. With the 3G GW detector network, it is possible to observe $\sim \mathcal{O}(1000)$ binary neutron star mergers per year that are localized well within one square degree in the sky for redshift $z \leqslant 0.3$. We show that 3G observatories will enable precision measurements of the BAO feature in the large-scale two-point correlation function; the effect of BAO can be independently detected at different redshifts, with a log-evidence ratio of ~ 23, 17, or 3, favoring a model with a BAO peak at redshift of 0.2, 0.25, or 0.3, respectively, using a redshift bin corresponding to a shell of thickness $150h^{-1}$ Mpc.

Unified Astronomy Thesaurus concepts: Gravitational wave astronomy (675); Gravitational wave detectors (676); Baryon acoustic oscillations (138); Large-scale structure of the universe (902); Cosmology (343); Gravitational wave sources (677); Gravitational waves (678)

1. Introduction

The catalog of gravitational wave (GW) transients from compact binary mergers has grown considerably (Abbott et al. 2019; Nitz et al. 2019; Venumadhav et al. 2020; Abbott et al. 2021b; Nitz et al. 2021) since the first detection of gravitational waves from the merger of the binary black hole GW150914 (Abbott et al. 2016). This growing catalog of mergers has already revolutionized our understanding of the astrophysical rates and populations of compact objects, and has enabled precision tests of general relativity and cosmology (Abbott et al. 2021a, 2021c). The sensitivity of the current ground-based GW detector network to compact binary mergers is expected to improve when the LIGO (Aasi et al. 2015), Virgo (Acernese et al. 2015), and KAGRA (Akutsu et al. 2021) detectors undergo upgrades (Abbott et al. 2018), and also with the construction of new detectors such as LIGO-India (Saleem et al. 2022). Additionally, third-generation (3G) detectors such as the Einstein Telescope (ET; Sathyaprakash et al. 2012) and Cosmic Explorer (CE; Reitze et al. 2019) will have an order-of-magnitude better strain sensitivity and will also be able to probe lower GW frequencies. It is also expected that they will localize most mergers within a few square degrees and detect hundreds of thousands of binary mergers each year (Mills et al. 2018). A number of precision tests of astrophysics and cosmology will be enabled as a result–for instance, studying the spatial distribution of a large number of well-localized sources, one can probe the large-scale distribution of matter in the universe (Vijaykumar et al. 2020; Cañas-Herrera et al. 2021; Libanore et al. 2021; Mukherjee et al. 2021a, 2021b). These probes using

GW observations could confirm if the distribution of GW mergers indeed tracks the galaxy distribution, and can provide an independent probe to the features mostly attributed to galaxy or quasar population, e.g., clustering bias (Kaiser 1984).

In this study, we investigate the possibility of probing another feature of the cosmological large-scale structure— baryon acoustic oscillations (BAOs)—with 3G GW detectors. The detection of a BAO peak with GW events can open up a complimentary window to probe cosmological parameters. GW detector networks are sensitive to mergers that occur in all directions in the sky. For redshift $z < 0.3$, where we expect that a large number of GW mergers are localized precisely enough (within one square degree), all the observed GW mergers can be used to probe the BAO feature and, unlike galaxy surveys, we will not be limited by the survey volume.

The layout of the paper is as follows: in Section 2 we give a brief overview of cosmological probes with GW observations, and explain why BAOs are an independent probe of large-scale structure. In Section 3 we describe the configurations of the 3G GW detector network used in this study. We describe our methodology for generating mock binary neutron star observations in Section 4, along with estimates of the measurability of the BAO feature in the correlation function. We conclude by summarizing our results and future directions in Section 5.

2. Cosmology and Gravitational Waves

Data from various cosmological surveys indicate that the evolution and current state of the universe are best described by the standard model of cosmology, also referred to as the ΛCDM model (Riess et al. 1998). This model includes dark energy (described by the cosmological constant Λ in Einstein's equations) as the dominant component, along with dark matter (a pressure-less fluid that interacts with standard model

particles purely through gravitational forces), and baryonic matter (which includes directly observable matter such as galaxies and the intergalactic medium). Given a cosmological model and a set of parameters, one can derive the relation between the distance to an astronomical object and the cosmological redshift z due to cosmic expansion. Conversely, independent measurements of the distances and z from observations can be turned into measurements of the cosmological model parameters.

In the last few years, a 4.4σ discrepancy has been reported between the value of the Hubble parameter H_0 measured using early universe (Aghanim et al. 2020) and late universe (Riess et al. 2019) probes, hinting either at unknown systematics in the measurements or at a "Hubble tension" and possible deviation from the ΛCDM paradigm. The independent measurement of the Hubble parameter using GWs from compact binaries is ideally suited to provide more clarity in this regard. The characteristic luminosity of GW sources provides a direct measurement of the luminosity distance out to the sources (Schutz 1986). If the redshift of these sources can be measured using any other methods, such as the detection of an electromagnetic counterpart (Holz & Hughes 2005; Dalal et al. 2006; Nissanke et al. 2013), statistical identification of the host galaxy using a galaxy catalog (Del Pozzo 2012; Chen et al. 2018), a measurement of the tidal parameter (Messenger & Read 2012; Chatterjee et al. 2021), or a physical scale in the mass distribution of sources (Farr et al. 2019; Ezquiaga & Holz 2021; You et al. 2021), one can measure the Hubble parameter. It is expected that a measurement accuracy of $\sim 4.4\%$ can be reached with ~ 250 binary neutron star merger detections (Gray et al. 2020).

Another avenue of study in cosmology where GW observations show promise is their use as tracers to study the large-scale structure of the universe. Similar to how galaxy surveys are used to probe large-scale clustering, a population of GW sources can be used to probe the cosmological large-scale structure by either the three-dimensional autocorrelation of the sources (Vijaykumar et al. 2020) or by cross-correlating the sources with other tracers of large-scale structure (Bera et al. 2020; Libanore et al. 2021; Mukherjee et al. 2021a, 2021b). These allow for constraints to be placed on the large-scale bias of gravitational wave events $b_{\rm GW}$, as well as on the parameters of the standard ΛCDM model of cosmology.

In this work, we ascertain the possibility of probing another feature in the large-scale clustering of matter, namely BAOs (Sakharov 1966; Peebles & Yu 1970; Sunyaev & Zeldovich 1970; Eisenstein & Hu 1998). BAOs are imprints left by early-time sound waves in the universe on the late-time distribution of matter. In the early universe (at redshifts >1089), high temperatures prevented the existence of bound atoms, and the primordial gas existed as ionized plasma. Free electrons in this plasma interacted with photons via Thomson scattering, thus coupling the baryons, electrons, and photons into an effective fluid. The competing forces of electromagnetic radiation pressure and gravity in this fluid generated perturbations, thus setting up sound waves in the fluid. During the epoch of recombination ($z \sim 1089$), the universe cooled down enough for stable atoms to form—this thwarted the Thomson scattering and destroyed the coupling. The photons then free-streamed and formed what we now know as the cosmic microwave background (CMB), while the perturbations froze at a certain scale. As the universe evolved
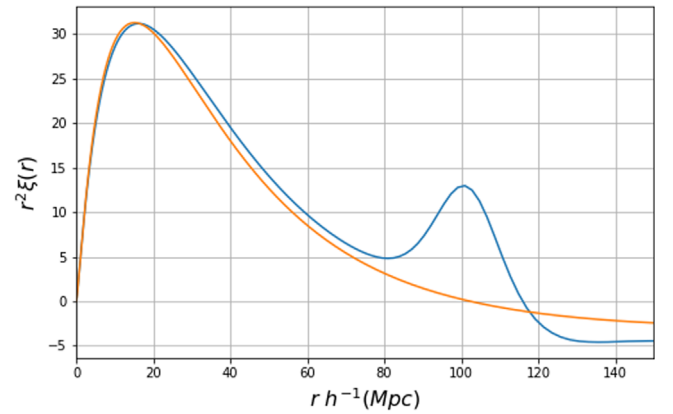

Figure 1. An example of two-point correlation function $\xi(r)$ as a function of comoving distance r. Here we show two correlation functions: (i) $\xi(r)$ showing a BAO feature at the scale of $\sim 100\ h^{-1}$Mpc is calculated using the transfer function prescribed by Eisenstein and Hu (Eisenstein & Hu 1998), and (ii) $\xi(r)$ without the BAO feature is calculated using the BBKS (Bardeen et al. 1986) transfer function. We assume ΛCDM cosmological model parameters consistent with the Planck 2015 data (Ade et al. 2016). We multiply the two-point correlation function $\xi(r)$ with r^2 on the vertical axis for a better visualization of the BAO peak. The units on the horizontal axis are h^{-1} Mpc, where h is defined in terms of the Hubble constant $H_0 = 100h$ km s^{-1} Mpc^{-1}.

and formed structures, this scale became imprinted on the distribution of halos and galaxies in the universe at late times, appearing as a peak in the two-point correlation function. For reviews on BAOs, see Bassett & Hlozek (2009) and Weinberg et al. (2013).

The first confident signature of BAOs from galaxy surveys came from the 3.4σ detection in the large-scale correlation function of luminous red galaxies from the Sloan Digital Sky Survey (SDSS) Data Release 3 (Eisenstein et al. 2005). These measurements have been confirmed by other samples such as the 6° Field Galaxy Survey (Beutler et al. 2011), the WiggleZ Dark Energy Survey (Blake et al. 2011a, 2011b), and most recently, by the SDSS-IV extended Baryon Oscillation Spectroscopic Survey (eBOSS; Bautista et al. 2020; Alam et al. 2021).

The BAO signature can be seen in the correlation function as a peak at a comoving scale of $\sim 100\ h^{-1}$ Mpc. In Figure 1, we show the three-dimensional correlation function $\xi(r)$ calculated using a transfer function fit provided by Eisenstein-Hu (Eisenstein & Hu 1998; with a BAO feature) and by Bardeen et al. (Bardeen et al. 1986), BBKS (without a BAO feature). This signature can also be captured by the two-point angular correlation function (2PACF) $w(\theta)$. Given a galaxy survey, one can estimate the correlation function using various estimators, most notably the Landy–Szalay estimator (Landy & Szalay 1993). For the localization volumes of typical binary mergers, the errors along the radial direction are larger than the errors in angular direction when these errors are converted into comoving length scales. It is hence convenient to measure the 2PACF from GW merger events, provided that the radial uncertainties are not large enough to smear away information in the correlation function at the scales of interest. In general, one needs to take into account the smearing of the measured correlation function due to localization errors (Vijaykumar et al. 2020) and projection effects (Limber 1954) to track the effective shape of 2PACF $w(\theta)$.

Table 1
The Specifications of Each Detector (Location, Noise Curves, Low-frequency Cutoff f_{low}) Considered in this Study

Abbreviation	Observatory	f_{low}	Noise Curve	Latitude	Longitude
C_1^U	Cosmic Explorer USA	5.2	CE1	40.8	−113.8
C_1^A	Cosmic Explorer Australia	5.2	CE1	−31.5	118.0
C_2^U	Cosmic Explorer USA	5.2	CE2	40.8	−113.8
C_2^A	Cosmic Explorer Australia	5.2	CE2	−31.5	118.0
E	Einstein Telescope	2	ET-D Design	43.6	10.5

Note. For the CE detector, subscripts (1, 2) represent (early, late) noise sensitivity curves, and superscripts (U, A) represent the location of these detector (USA, Australia). These detector configurations for CE and ET are taken from Nitz & Dal Canton (2021).

3. Third-generation Detector Network

The proposed 3G detectors such as CE (Reitze et al. 2019; Evans et al. 2021) and ET (Punturo et al. 2010) are expected to be operational sometime in next decade (2030s). CE is proposed to be built in two stages with an upgrades consisting of increasing design complexity and better sensitivity, known as CE1 and CE2 (Hall et al. 2021). ET is proposed to have good sensitivity at low frequency (Hild et al. 2011); we consider the design sensitivity $f_{\text{low}} = 2$ Hz of ET for this study. The locations of these detectors are not yet finalized, but we use a fiducial location for these detectors: one CE in the USA, and the other CE in Australia, which provides a long baseline. These fiducial detector locations have also been used in previous works (Hall & Evans 2019; Nitz & Dal Canton 2021). We consider the location of ET to be in Europe. Table 1 lists the properties of the detectors we consider in this study. In this study, we focus on the localization capabilities of the 3G detector network only. Any 2G detector(s) added to the network would only further enhance the localization capabilities of the network. We consider the following detector network configurations:

1. $C_1^U C_1^A E$: Two CE detectors (one in the USA, and the other in Australia) and ET (in Europe), where the CE detectors have the early phase design sensitivity CE1, and
2. $C_2^U C_2^A E$: Same as above, but a CE with the second phase design sensitivity CE2.

Although we examine these specific configurations of the worldwide detector network, we do not expect other detector network configurations to change the distribution of the localization errors of BNS events significantly as long as they include several next-generation observatories.

4. Simulations and Results

Next-generation detectors will significantly improve the localization for both BNS and BBH mergers, and due to the higher intrinsic merger rates, we expect to obtain a much larger number of BNS events with highly precise localization volumes at low redshift ($z < 0.3$). Although we only consider BNS simulations in this study, our method can readily be generalized to BBHs.

We create a fiducial universe containing localization posteriors for BNS events observed with 3G detector networks, and we call it a BNS catalog. To assemble this BNS catalog, we create a realization of the universe containing a large number of galaxies (fiducial galaxy catalog), a (randomly selected) small fraction of which can act as host galaxies to BNS events. These galaxies need to be distributed spatially in such a way that the

underlying correlation function contains the BAO peak, as shown in Figure 1.

4.1. BNS Population Distribution

To generate a realistic population of BNS, we use the Madau-Dickinson star formation rate (SFR) $\psi(z)$ (Madau & Dickinson 2014),

$$\psi(z) = 0.015 \frac{(1 + z)^{2.7}}{1 + [(1 + z)/2.9]^{5.6}} \, M_\odot \, \text{yr}^{-1} \, \text{Mpc}^{-3} \quad (1)$$

.We assume that the local formation rate of the BNS is proportional to the SFR. To derive the merger rate, the SFR is corrected with a delay-time distribution $p(t_D) \sim 1/t_D \sim 1/(t - t_f)$, where t_f is the formation time of the binary,

$$\Psi(z) = \int_{z_f}^{z} \psi(z') \, P(t(z') - t_f) dz' \quad (2)$$

.This choice of the delay-time distribution is motivated by classical isolated binary evolution models (O'Shaughnessy et al. 2010; Dominik et al. 2012). We normalize Equation (2) such that $\Psi(z = 0)$ gives us the local merger rate of 320 yr^{-1}Gpc^{-3}, the median estimated merger rate of BNS mergers from GWTC-2 (Abbott et al. 2021d). In the detector frame, the number density of of BNS mergers dN/dz is related to the source frame merger rate $\Psi(z)$ by the following relation,

$$\frac{dN}{dz} = \frac{dV_c}{dz} \frac{\Psi(z)}{1 + z} \quad (3)$$

,

where V_c is the comoving volume. We integrate Equation (3) in a given redshift bin and estimate the total number of BNS mergers $\Delta \mathcal{N}(z)$ expected in that redshift bin from 3G detectors. The results we thus obtain are consistent with Mills et al. (2018).

4.2. Parameter Estimation

To estimate the localization posterior for each simulated BNS source, we make use of Bayesian parameter estimation technique using a publicly available code PyCBC Inference (Biwer et al. 2019). We distribute nonspinnning BNS sources assuming the source frame component masses to be equal to 1.4 $M_\odot$. Since the mass distribution of neutron stars is narrow, we do not expect the results of the study to differ significantly from any other mass distributions for BNS sources. We assume that the sources are distributed isotropically in the sky and orientation for the inclination angle, and uniformly in comoving distance. The redshift (or distance)

distribution can be obtained by rescaling the base population to the desired rate as a function of redshift such as in Equation (3). We use the heterodyne likelihood model (Cornish 2010; Zackay et al. 2018; Finstad & Brown 2020) to estimate the likelihood function. We choose the following parameters to vary in the parameter estimation: the chirp mass $\mathcal{M}$, the mass ratio q, $(q > 1)$, the inclination angle, the luminosity distance D_L, the R.A. and decl. dec, the polarization angle, and the merger time: t_c. We use uniform priors on $\mathcal{M}$ (detector frame), q, and t_c and isotropic priors for R.A., decl., inclination angle, and polarization. For distance, we choose a prior uniform in comoving volume. We use the TAYLORF2 waveform model (Blanchet et al. 1995; Faye et al. 2012) implemented in LALSUITE (LALSuite 2020) to simulate our signal in Gaussian noise and for the signal recovery while estimating the source parameters. TAYLORF2 excludes the merger from the analysis, but we still recover a significant signal-to-noise ratio (S/N) due to the long signal length and enhanced low-frequency sensitivity of the 3G detectors. Due to the significantly low-frequency cutoff of ET ($f_{low} \sim 2$ Hz), the length of the signal is very long, and hence we take Earth rotation effects into account. We sample the signal at 1024 Hz, and introduce a high-frequency cutoff of 512 Hz to evaluate the likelihood function in order to reduce the computational cost. Ideally, the high-frequency cutoff should be much larger, but this does not cause a significant loss in S/N compared to the full signal, and we are still able to obtain highly localized posteriors for the redshift range we are interested in. To sample over the parameters, we use a sampler based on a dynamical nested sampling algorithm (Skilling 2006; Higson et al. 2019) implemented in the software package DYNESTY(Speagle 2020).

4.3. Methodology

For the purposes of this study, we assume that BNS events are hosted by galaxies, and hence they trace the underlying galaxy distribution. To create a realization of BNS events that trace the galaxy distribution, we first choose a shell centered around the redshift we are interested in, and generate an underlying fiducial galaxy catalog. The density of the selected BNS events depends on the total number of mergers expected in the shell, with the additional condition that they should be localized within one square degree. Figure 2 shows the number of events that satisfy this criterion as a function of redshift.

To generate the fiducial galaxy catalogs, we use the publicly available code lognormal_galaxies (Agrawal et al. 2017). The input power spectrum is calculated using the Eisenstein and Hu transfer function (Eisenstein & Hu 1998), which contains the BAO peak. We assume a standard ΛCDM cosmology with parameters consistent with Planck results (Ade et al. 2016). After constructing the galaxy catalog, host galaxies are chosen randomly and localization posteriors are placed according to the errors obtained from simulations. In Figure 3 we illustrate a realization of one such BNS catalog with marginalized posteriors for the localization parameters. Each BNS catalog consists of N posterior samples combined to give a posterior field $\mathcal{P} = \sum_{i=1}^{N} \mathcal{P}_i(\text{R.A.}, \text{decl.}, D_C)$, where $\mathcal{P}_i$ is the individual localization posterior for R.A., decl., and the comoving distance D_c.

Once we have a BNS catalog at a given redshift, to extract the BAO peak, we focus on a shell of thickness $\approx 150\ h^{-1}$ Mpc at redshifts $z = \{0.2, 0.25, 0.3\}$. We use the following algorithm to extract the BAO peak:
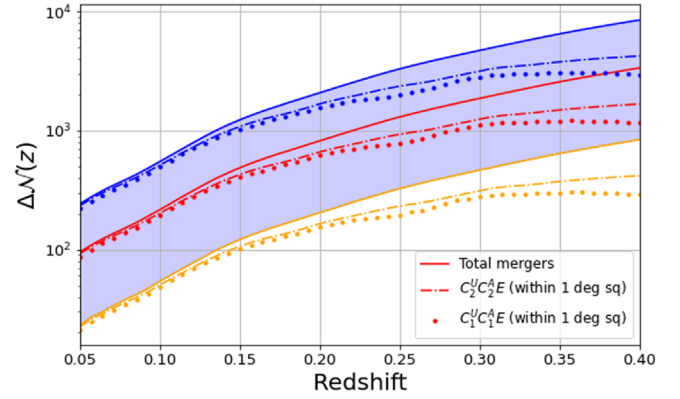

Figure 2. The number of BNS mergers per year in a shell of thickness 150 h^{-1} Mpc as a function of redshift. Solid lines represent the total number of mergers, dot-dashed and dashed lines represent the BNS mergers with a sky localization within 1 square degree in that shell for the two-detector network (see the text for explanation). The red lines represent the mean number of BNS mergers in the shell per year, corresponding to the mean value of the merger rate. Similarly, the blue (yellow) lines represent the upper (lower) limits on the number of BNS mergers corresponding to the upper (lower) limits of BNS merger rate. The shaded blue region represents the range of values that the number of mergers can take between these upper and lower limits. Solid lines represent the total number of mergers, while dash-dotted and dotted lines represent the total number of detectable events with sky localization errors <1 deg^2 for different detector networks considered.

1. For a given redshift, choose a shell of thickness ∼150 h^{-1} Mpc in comoving volume. To avoid the autocorrelation of points from the same posterior, randomly select one point from each posterior that lies within the chosen shell. This is the optimal choice, as a larger shell will wash away the BAO peak and a smaller shell will not have enough events to estimate the 2PACF with enough precision.

2. Use the selected points to calculate 2PACF using the Landy–Szalay estimator, i.e.,

$$w_i(\theta) = \frac{DD_i(\theta) - 2DR_i(\theta) + RR_i(\theta)}{RR_i(\theta)} ,\qquad (4)$$

where $DD_i(\theta)$ is the number of pairs of data points in the bin separated by angle θ, $RR_i(\theta)$ is the number of point-pairs in an equal-sized random catalog separated by θ, and $DR_i(\theta)$ is the number of data-random pairs separated by θ. We use the publicly available code CORRFUNC (Sinha & Garrison 2019, 2020) to calculate the correlation function. To minimize the projection effects in the shell, we divide the shell of 150 h^{-1} Mpc into smaller subshells of 60 h^{-1} Mpc with a sliding window of 30 h^{-1} Mpc and take the average.

3. Repeat the above procedure for different realizations of the posterior field (by randomly selecting a point from each posterior) and estimate the average 2PACF $w(\theta) = \frac{1}{n}\sum_{i=1}^{n} w_i(\theta)$. For this study, we chose $n = 100$ for each subshell of 60 h^{-1} Mpc.

4. Once we have recovered $w(\theta)$, we model the 2PACF following (Sanchez et al. 2011)

$$w(\theta) = A + B\theta^\nu + C \exp\left[-\frac{(\theta - \theta_{\text{FIT}})^2}{2\sigma_{\text{FIT}}^2}\right]\qquad (5)$$

.This model has six parameters to fit the data: $\{A, B, C, \nu, \theta_{\text{FIT}}, \sigma_{\text{FIT}}\}$. The first two terms in the model give the power law to fit the broad shape of the correlation
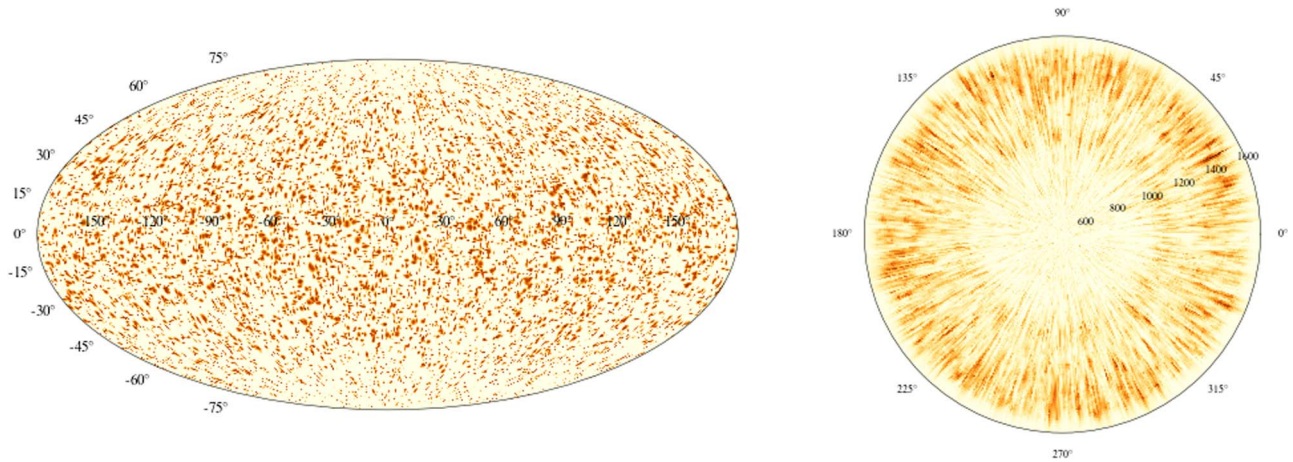
Figure 3. A realization of combined posterior field for the marginalized localization posterior from the simulation of BNS events using the 3G detector network. The left panel shows the marginalized posteriors for R.A. (R.A.) and decl. (decl.) angles. The right panel shows the marginalized posteriors on R.A. and comoving distance (along the radial direction).

function, and the last term models the BAO peak as a Gaussian with a location of the peak as θ_{FIT} and with a width of the peak as σ_{FIT} along with the amplitude C. To fit a model without a BAO peak, we drop the last term in Equation (5) and fit for the remaining three parameters.

5. To account for systematic and statistical errors, we generate 50 galaxy catalogs for each redshift, corresponding to different seeds for the underlying density field. We then take 20 realizations from each galaxy catalog to account for statistical fluctuation in choosing the set of host galaxies. In this way, we account for errors due to cosmic variance, errors arising from the sampling bias due to the selection of the host galaxies, and errors due to localization posteriors.

We do not correct the recovered 2PACF $w(\theta)$ for (i) smearing effects due to localization errors or for (ii) projection effects in a shell. This is justified because we do not track the exact shape of 2PACF. Rather, we are interested in the location of the BAO peak in the 2PACF. As long as these effects do not destroy the BAO peak in the correlation function, we should be able to recover it. The recovery of the BAO peak with BNS merger events is also a statistical effect: one can confuse a statistical bump in the correlation function with the BAO peak. In order to confidently recover the BAO peak, one must consider recovering the BAO peak in various redshift bins.

4.4. Results

In Figure 4 we show the recovery of the BAO peak in one realization of BNS merger events at redshift $z = 0.3$. We estimate the input angular BAO scale at a given redshift z using the relation $\theta_{\mathrm{BAO}} = r_s/((1+z)D_A(z))$, where r_s is the BAO scale in terms of comoving distance, and $D_A(z)$ is the angular diameter distance to the given redshift. For this BNS catalog, we fit the models with and without a BAO peak using the software package DYNESTY (Speagle 2020). We estimate the Bayesian evidence $\mathcal{Z}$ for both models and compare them. The model with the higher value (>2.5) of $\mathcal{Z}$ is statistically preferred (Jeffreys 1998). The difference in log evidence between the two models turns out to be $\ln(\mathcal{Z}_1/\mathcal{Z}_2) = 2.59$, indicating that the model with a BAO peak is favored compared to the model without a BAO peak.
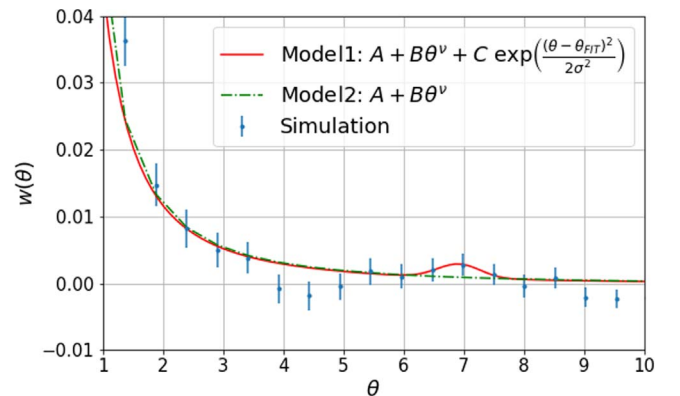

Figure 4. 2PACF recovery is shown here for a realization at redshift $z = 0.3$. We also show the fit to the data using the model described in the text. The input value for θ_{BAO} for $z = 0.3$ is 6.9. We estimate the difference in log evidence for both models as $ln\frac{Z1}{Z2} = 2.59$, indicating that model with a BAO peak is favored compared to the model without a BAO peak. The errors are obtained by averaging over 1000 catalogs, which accounts for the sampling bias due to the selection of galaxies for BNS merger events, cosmic variance, and due to scatter in the localization posteriors.
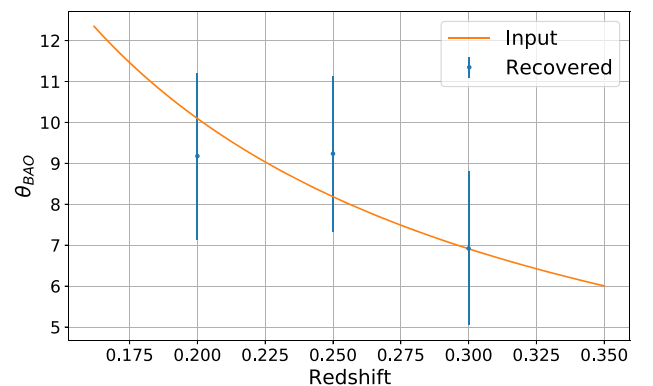

Figure 5. The recovery of the BAO scale at different redshifts. The solid continuous line shows the angular BAO scale as a function of redshift. The errors on the recovered BAO scale are estimated from averaging over 1000 catalogs to account for cosmic variance as well as statistical errors due to selecting host galaxies for BNS merger events from large galaxy catalogs. We estimate the difference in the log evidence for the fit function for two models (with BAO and without BAO). For all the redshifts, the model with a BAO peak is favored (see text).
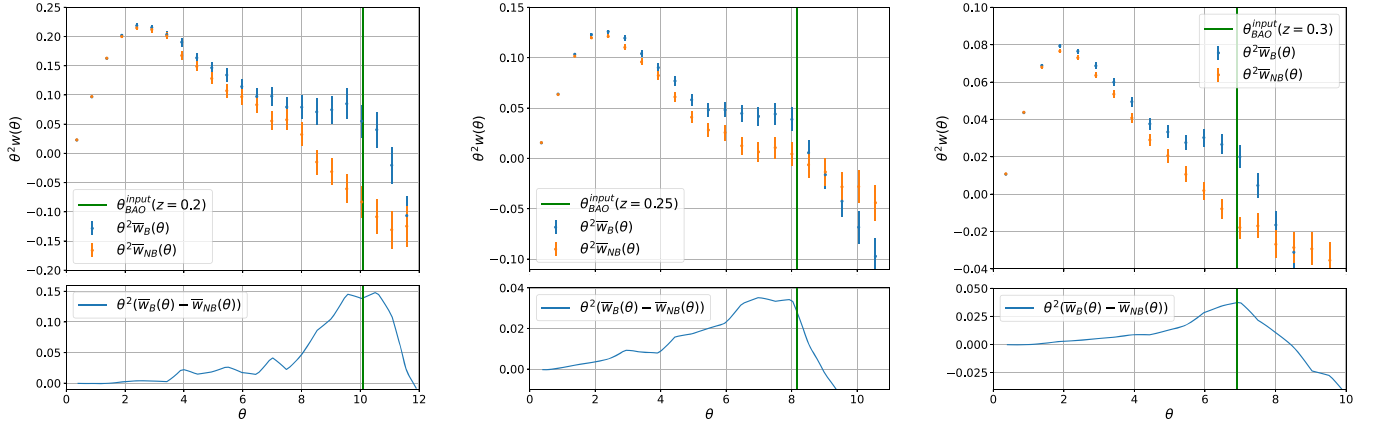
Figure 6. The average of the 2PACF for all the BNS catalogs. $\overline{w}_B(\theta)$ represents the average for all the catalogs that contain a BAO peak, and $\overline{w}_{NB}(\theta)$ is the same for the catalogs without a BAO peak. In the upper panels, we show the 2PACF for both sets of catalogs. The solid vertical line shows the input angular BAO scale at the given redshift. In the lower panel, we show the difference in the average correlation functions obtained from both sets of catalogs. We show the quantity $\theta^2\overline{w}(\theta)$ on the vertical axis to better visualize the BAO peak. The three figures are shown for redshifts $z = 0.2$ (left panel), 0.25 (middle panel), and 0.3 (right panel).

In Figure 5 we show the the recovery of the BAO peak at different redshift bins. We estimate the Bayesian evidence for both models in these redshift bins. The $\ln(\mathcal{Z}_1/\mathcal{Z}_2)$ for these redshift bins is given by $23.29 (z = 0.2)$, $16.73 (z = 0.25)$, and $2.59 (z = 0.3)$, again indicating that the model with a BAO peak is favored. We show that with 7–10 yr of observation, enough BNS merger events can be accumulated to recover the BAO peak within the statistical errors.

For these simulations, the significant budget in errors arises from the sampling bias and due to cosmic variance. Scatter due to posterior samples contributes least to the error budget. However, this would change at higher redshift, where localization errors become dominant due to the large scatter in the localization posteriors. The errors due to sampling bias will decrease when the number of detections is increased, for example, due to higher merger rates.

To check the robustness of the method, we also generate ∼1000 BNS catalogs from the corresponding galaxy catalogs that do not contain a BAO peak. We use the BBKS transfer function (Bardeen et al. 1986) to calculate the input correlation function to generate these catalogs. We then estimate the average 2PACF $w(\theta)$ across all catalogs in the respective categories (with a BAO peak and without a BAO peak). In Figure 6 we show the average of the 2PACF estimated from all the BNS merger catalogs in two categories, (i) those containing a BAO peak, and (ii) those without a BAO peak. It can be seen that statistically, we recover the BAO peak at the injected value. In these simulations, we find that the redshift window between $z \in [0.2, 0.3]$ is best suited for our study because we obtain a large number of BNS events with the desired localization accuracy. Beyond $z > 0.3$, although we do obtain enough BNS events that are localized within a degree square, the localization errors along the radial direction start to dominate and become large enough to destroy the angular correlations as well. Since the BAO feature is very weak and is hard to detect, to account for statistical fluctuations, it is preferable to recover the BAO feature in 2PACF in a sliding window of a given shell thickness in the ideal redshift range described above.

These measurements in GW catalogs, apart from being independent probes of the BAO scale, provide the opportunity of constraining the cosmological parameters by using the BAO

scale as a standard ruler. At the low redshifts of interest in this study, r_s is a direct measure of the Hubble parameter H_0. Using the r_s and $\Omega_m h^2$ (where $h = H_0/100$) derived from CMB experiments in conjunction with the measurements from GW data, one can measure the value of Ω_m (Eisenstein et al. 1998). Alternatively, the measurements of the BAO scale θ_{BAO} at different redshifts can be used to measure r_s (Carvalho et al. 2016).

Although we use a GW detector network consisting only of 3G detectors, it is also possible that many current ground-based detectors will still be in operation (with future upgrades). This scenario will only improve the localization of sources, and hence a hybrid network consisting of 3G detectors such as CE and ET, and 2G detectors such as LIGO, Virgo, and KAGRA, will greatly improve the localization of the GW sources.

In this study, we assumed that the network of detectors will have the same sensitivity for all sky positions. Depending on the given network configuration and antenna pattern, we might obtain a varying sensitivity for different parts of sky. Although we expect this effect to be small for 3G detectors, one natural extension of this work is to include these effects. However, in the future, we intend to extend this work to include smearing effects due to posteriors (Vijaykumar et al. 2020), projection effects due to the shell thickness (Limber 1954), and more current-generation detectors along with 3G detector networks. The conclusions of the current work also rely on the range of estimated merger rates of BNS events (Abbott et al. 2021b). A future increase (decrease) in the estimation of merger rates would mean that less (more) time will be required to accumulate enough BNS merger events to probe BAO.

5. Summary

We explore the possibility of detecting the BAO scale using GW merger events in the 3G detector network. Probing the details of large-scale structures (e.g., the BAO scale) with GW observations is a challenging task because of the poor localization of the GW sources and the low number density of detected events. We find that with a 3G detector network consisting of two CEs (in the USA and in Australia) and one ET (in Europe), we can accumulate a large number ($\mathcal{O}(10,000)$) of very well localized (within one square degree) BNS events up to redshift ($z < 0.3$) in 7–10 yr of observing time. This

opens up the possibility of probing the BAO scale solely by GW observations and hence provides an independent probe for BAOs. With the 3G detector network considered in this study, we find that the redshift range of $z \in [0.2, 0.3]$ is best suited for a recovery of a BAO peak assuming that the GW merger population does track the galaxy distribution. We showed this through simulations at three different redshifts—0.2, 0.25, and 0.3—by considering a small shell of thickness $150h^{-1}$ Mpc centered around each redshift. In reality, when we accumulate enough BNS events in this redshift range, we can divide it into many smaller redshift bins to estimate the 2PACF and infer the presence of the BAO peak in each bin. The new probe for BAOs will not only complement the observations from other surveys, it may provide the opportunity of peeking into the distribution of BNS with relation to galaxies and provide independent constraints on cosmological parameters. This study broadens the horizon of the science goals that can be achieved with 3G detectors and emphasizes the need for a 3G detector network for the future.

We made a few simplifying assumptions for the purpose of this work. As a proof of concept, we only considered BNSs and their localization at low redshifts. We reiterate that this choice is based purely on the measured relative intrinsic merger rates of BBHs and BNSs and on their localization volumes. If the numbers and localization volumes of BBHs are comparable to those considered in this study at some redshifts, the methods described will translate trivially.

We also assumed that all galaxies in our mock catalog would host BNS events with equal probability; however, more massive/luminous galaxies are expected to be preferred hosts for BNS events. Hence, ideally, one should have weighted the galaxies by their mass while populating them with BNSs. We expect the mass weighting to affect the measured large-scale bias of GW events since the bias is known to strongly depend on of galaxy luminosity (Zehavi et al. 2005). However, we expect the errors introduced on the position and shape of the BAO peak (less than 1%; Smith et al. 2007) to be subdominant to the measurement errors in the 2PACF.

Last, we restricted ourselves to using the 2PACF in order to measure clustering. An equivalent analysis could also be performed using angular power spectra (Peebles 1973), as is done for other cosmological probes. We plan to investigate this thoroughly, along with the effects mentioned in the preceding paragraphs, in future work.

ORCID iDs

Sumit Kumar https://orcid.org/0000-0002-6404-0517
Aditya Vijaykumar https://orcid.org/0000-0002-4103-0666
Alexander H. Nitz https://orcid.org/0000-0002-1850-4587

References

Aasi, J., Abbott, B. P., Abbott, R., et al. 2015, CQGra, 32, 074001
Abbott, B., Abbott, R., Abbott, T., et al. 2016, PhRvD, 93, 12003
Abbott, B. P., Abbott, R., Abbott, T. D., et al. 2018, LRR, 21, 3
Abbott, B. P., Abbott, R., Abbott, T. D., et al. 2019, PhRvX, 9, 031040
Abbott, B. P., Abbott, R., Abbott, T. D., et al. 2021a, ApJ, 909, 218
Abbott, R., Abbott, T. D., Abraham, S., et al. 2021b, PhRvX, 11, 021053
Abbott, R., Abbott, T. D., Abraham, S., et al. 2021c, PhRvD, 103, 122002
Abbott, R., Abbott, T. D., Abraham, S., et al. 2021d, ApJL, 913, L7
Acernese, F., Agathos, M., Agatsuma, K., et al. 2015, CQGra, 32, 024001
Ade, P. A. R., Aghanim, N., Arnaud, M., et al. 2016, A&A, 594, A13
Aghanim, N., Akrami, Y., Ashdown, M., et al. 2020, A&A, 641, A6
Agrawal, A., Makiya, R., Chiang, C.-T., et al. 2017, JCAP, 2017, 003003
Akutsu, T., Ando, M., Arai, K., et al. 2021, PTEP, 2021, 05A101
Alam, S., Aubert, M., Avila, S., et al. 2021, PhRvD, 103, 083533
Bardeen, J. M., Bond, J. R., Kaiser, N., & Szalay, A. S. 1986, ApJ, 304, 15
Bassett, B. A., & Hlozek, R. 2009, in Dark Energy: Observational and Theoretical Approaches, ed. P. Ruiz-Lapuente (Cambridge, UK: Cambridge Univ. Press)
Bautista, J. E., Paviot, R., Magaña, M. V., et al. 2020, MNRAS, 500, 736
Bera, S., Rana, D., More, S., & Bose, S. 2020, ApJ, 902, 79
Beutler, F., Blake, C., Colless, M., et al. 2011, MNRAS, 416, 3017
Biwer, C. M., Capano, C. D., De, S., et al. 2019, PASP, 131, 024503
Blake, C., Kazin, E., Beutler, F., et al. 2011a, MNRAS, 418, 1707
Blake, C., Davis, T., Poole, G., et al. 2011b, MNRAS, 415, 2892
Blanchet, L., Damour, T., Iyer, B. R., Will, C. M., & Wiseman, A. G. 1995, PhRvL, 74, 3515
Carvalho, G. C., Bernui, A., Benetti, M., Carvalho, J. C., & Alcaniz, J. S. 2016, PhRvD, 93, 023530
Cañas-Herrera, G., Contigiani, O., & Vardanyan, V. 2021, ApJ, 918, 20
Chatterjee, D. R., Aa, A. H. K., Holder, G., et al. 2021, PhRvD, 104, 083528
Chen, H.-Y., Fishbach, M., & Holz, D. E. 2018, Natur, 562, 545
Cornish, N. J. 2010, arXiv:1007.4820
Dalal, N., Holz, D. E., Hughes, S. A., & Jain, B. 2006, PhRvD, 74, 063006
Del Pozzo, W. 2012, PhRvD, 86, 043011
Dominik, M., Belczynski, K., Fryer, C., et al. 2012, ApJ, 759, 52
Eisenstein, D. J., & Hu, W. 1998, ApJ, 496, 605
Eisenstein, D. J., Hu, W., & Tegmark, M. 1998, ApJL, 504, L57
Eisenstein, D. J., Zehavi, I., Hogg, D. W., et al. 2005, ApJ, 633, 560
Evans, M., Adhikari, R. X., Afle, C., et al. 2021, arXiv:2109.09882
Ezquiaga, J. M., & Holz, D. E. 2021, ApJL, 909, L23
Farr, W. M., Fishbach, M., Ye, J., & Holz, D. 2019, ApJL, 883, L42
Faye, G., Marsat, S., Blanchet, L., & Iyer, B. R. 2012, CQGra, 29, 175004
Finstad, D., & Brown, D. A. 2020, ApJL, 905, L9
Gray, R., Hernandez, I. M., Qi, H., et al. 2020, PhRvD, 101, 122001
Hall, E. D., & Evans, M. 2019, CQGra, 36, 225002
Hall, E. D., Kuns, K., Smith, J. R., et al. 2021, PhRvD, 103, 122004
Higson, E., Handley, W., Hobson, M., & Lasenby, A. 2019, S&C, 29, 891
Hild, S., Abernathy, M., Acernese, F., et al. 2011, CQGra, 28, 094013
Holz, D. E., & Hughes, S. A. 2005, ApJ, 629, 15
Jeffreys, H. 1998, The Theory of Probability (Oxford Classic Texts in the Physical Sciences) (3rd ed.; Oxford: Oxford Univ. Press)
Kaiser, N. 1984, ApJL, 284, L9
Landy, S. D., & Szalay, A. S. 1993, ApJ, 412, 64
Libanore, S., Artale, M. C., Karagiannis, D., et al. 2021, JCAP, 02, 035
LALSuite 2020, LSC Algorithm Library Suite,
Limber, D. N. 1954, ApJ, 119, 655
Madau, P., & Dickinson, M. 2014, ARA&A, 52, 415
Messenger, C., & Read, J. 2012, PhRvL, 108, 091101
Mills, C., Tiwari, V., & Fairhurst, S. 2018, PhyRv, D97, 104064
Mukherjee, S., Wandelt, B. D., Nissanke, S. M., & Silvestri, A. 2021a, PhRvD, 103, 043520
Mukherjee, S., Wandelt, B. D., & Silk, J. 2021b, MNRAS, 502, 1136
Nissanke, S., Holz, D. E., Dalal, N., et al. 2013, arXiv:1307.2638
Nitz, A. H., Capano, C. D., Kumar, S., et al. 2021, ApJ, 922, 76
Nitz, A. H., & Dal Canton, T. 2021, ApJL, 917, L27
Nitz, A. H., Dent, T., Davies, G. S., et al. 2019, ApJ, 891, 123
O'Shaughnessy, R., Kalogera, V., & Belczynski, K. 2010, ApJ, 716, 615
Peebles, P. J. E. 1973, ApJ, 185, 413
Peebles, P. J. E., & Yu, J. T. 1970, ApJ, 162, 815
Punturo, M., Abernathy, M., Acernese, F., et al. 2010, CQGra, 27, 194002
Reitze, D., Adhikari, R. X., Ballmer, S., et al. 2019, BAAS, 51, 035
Riess, A. G., Casertano, S., Yuan, W., Macri, L. M., & Scolnic, D. 2019, ApJ, 876, 85
Riess, A. G., Filippenko, A. V., Challis, P., et al. 1998, AJ, 116, 1009

Sakharov, A. D. 1966, JETP, 22, 241
Saleem, M., Rana, J., Gayathri, V., et al. 2022, CQGra, 39, 025004
Sanchez, E., Carnero, A., Garcia-Bellido, J., et al. 2011, MNRAS, 411, 277
Sathyaprakash, B., Abernathy, M., Acernese, F., Ajith, P., & Allen, B. 2012, CQGra, 29, 124013
Schutz, B. F. 1986, Natur, 323, 310
Sinha, M., & Garrison, L. H. 2019, in Software Challenges to Exascale Computing. Second Workshop, SCEC 2018, Vol. 964, ed. A. Majumdar & R. Arora (Singapore: Springer), 3
Sinha, M., & Garrison, L. H. 2020, MNRAS, 491, 3022
Skilling, J. 2006, BayAn, 1, 833
Smith, R. E., Scoccimarro, R., & Sheth, R. K. 2007, PhRvD, 75, 063512

Speagle, J. S. 2020, MNRAS, 493, 3132
Sunyaev, R. A., & Zeldovich, Y. B. 1970, Ap&SS, 7, 3
Venumadhav, T., Zackay, B., Roulet, J., Dai, L., & Zaldarriaga, M. 2020, PhRvD, 101, 083030
Vijaykumar, A., Saketh, M. V. S., Kumar, S., Ajith, P., & Choudhury, T. R. 2020, arXiv:2005.01111
Weinberg, D. H., Mortonson, M. J., Eisenstein, D. J., et al. 2013, PhR, 530, 87
You, Z.-Q., Zhu, X.-J., Ashton, G., Thrane, E., & Zhu, Z.-H. 2021, ApJ, 908, 215
Zackay, B., Dai, L., & Venumadhav, T. 2018, arXiv:1806.08792
Zehavi, I., Zheng, Z., Weinberg, D. H., et al. 2005, ApJ, 630, 1